

Diffraction theory: application of the fast Fourier factorization to cylindrical devices with arbitrary cross section lighted in conical mounting

Philippe Boyer, Evgeny Popov, Michel Nevière, and Gilles Renversez

Institut Fresnel, Case 161, Unité Mixte de Recherche Associée au Centre National de la Recherche Scientifique (UMR 6133), Université Paul Cézanne Aix-Marseille III, et Université de Provence, Faculté des Sciences et Techniques de St. Jérôme, Avenue Escadrille Normandie Niémen, 13397 Marseille Cedex 20, France

Received May 2, 2005; revised October 7, 2005; accepted October 10, 2005; posted November 16, 2005 (Doc. ID 61886)

The differential theory of diffraction by arbitrary cross-section cylindrical objects is developed for the most general case of an incident field with a wave vector outside the cross-section plane of the object. The fast Fourier factorization technique recently developed for studying gratings is generalized to anisotropic and/or inhomogeneous media described in cylindrical coordinates; thus the Maxwell equations are reduced to a first-order differential set well suited for numerical computation. The resolution of the boundary-value problem, including an adapted *S*-matrix propagation algorithm, is explained in detail for the case of an isotropic medium. Numerical applications show the capabilities of the method for resolving complex diffraction problems. The method and its numerical implementation are validated through comparisons with the well-established multipole method. © 2006 Optical Society of America

OCIS codes: 050.1960, 060.0060.

1. INTRODUCTION

Cylindrical devices commonly appear in diffraction and propagation theory, and their interest has recently increased with the advent of microstructured optical fibers (MOFs).¹ An efficient method called the multipole method (MM) has already been developed to study devices composed of cylindrical inclusions.^{1–3} Nevertheless, it has at least two major limitations: All the inclusions must be included in nonoverlapping circles and the refractive index of the matrix containing the inclusions must be homogeneous. In addition, the reflection matrix relating the incident and the scattered field for each individual inclusion must be obtained by other means in the case of a noncircular inclusion or inhomogeneous circular inclusion. In what follows, we present the application of the fast Fourier factorization (FFF) method to diffraction theory. This new method has none of the known limitations of the MM. Briefly, the FFF method rewrites the Maxwell equations through the use of a Fourier series. Although an isolated cylindrical object is *a priori* nonperiodic, it becomes 2π periodic with respect to the polar angle θ when it is described in cylindrical coordinates. This periodicity allows us to describe both the electromagnetic field and the diffracting object in terms of a Fourier series. As was previously done in grating theory,⁴ it is now possible to reduce the Maxwell equations to a first-order differential set that must be numerically integrated. Of course the numerical treatment requires truncating the Fourier series of the field, a process that has created great numerical problems for decades but recently received a solution through what is now called the FFF method. In a recent paper⁵ we proved that such a method was able to give fast

converging results when a cylindrical object was illuminated under TM polarization. The aim of the present paper is to extend the theory to the most general case in which the diffraction device is illuminated with a field propagating outside the cross-section plane of the device, which leads to a full vectorial problem that does not reduce to the two classical TE and TM cases of polarizations. Moreover, the propagation equations will be derived in anisotropic media to open a way to resolve the diffraction problem of a wave by an arbitrary cylinder made of an arbitrary (lossy or lossless) anisotropic medium. In Sections 2 and 3 we present the FFF principles to obtain the set of differential equations defined in the area where the diffracting device locates. In Section 4 we discuss the complete solution of the diffracting problem in the case of an isotropic medium. In some cases, the diffracting object is invariant by a rotation of angle $T=2\pi/N_T$ (N_T is the number of subperiods of the 2π range). In Section 5 the numerical theory is adapted to take into account this subperiodicity on the T range of the polar angle coordinate θ . Finally, we validate the numerical implementation of our method with the well-established MM (Refs. 2 and 3) through several examples including the excitation of the fundamental mode of a six-hole MOF; we also discuss some aspects of the numerical efficiency and accuracy of the FFF method.

2. PRESENTATION OF THE PROBLEM

We consider a cylindrical object described in both a Cartesian coordinate system $Oxyz$ with $(\mathbf{e}_x, \mathbf{e}_y, \mathbf{e}_z)$ unit vectors and in cylindrical coordinates r, θ, z with $(\mathbf{e}_r, \mathbf{e}_\theta, \mathbf{e}_z)$ as

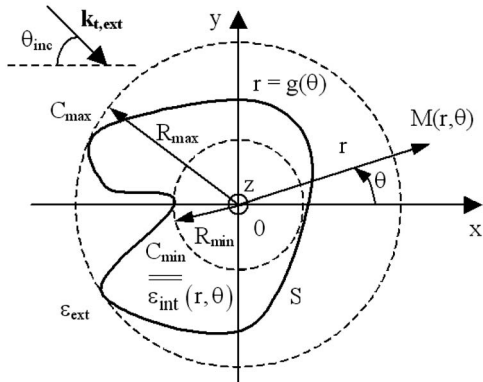


Fig. 1. Cross section of an arbitrary shaped cylindrical object filled with an anisotropic and inhomogeneous media and described by a directrix $r=g(\theta)$ containing the origin in the Oxy plane and generatrices parallel to the z axis.

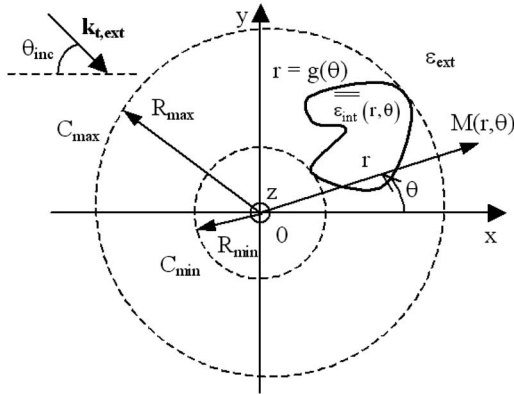


Fig. 2. Same kind of arbitrary cross section as in Fig. 1 with the origin outside the directrix.

unit vectors. Its surface (S) is defined by an arbitrary directrix located in the cross-section plane (Oxy) containing the origin as shown in Fig. 1 or outside the origin (see Fig. 2). Generatrices are straight lines parallel to the z axis. The equation of the directrix is $f(r, \theta)=0$ or $r=g(\theta)$, in which f and g are given functions. The surface (S) divides the space into two regions. The first one, the internal region denoted int, is contained inside the surface and is filled with a linear, inhomogeneous and anisotropic medium, dielectric or conducting (nonmagnetic), and its complex permittivity tensor is denoted $\overline{\overline{\epsilon}}_{int}(r, \theta)$. The second region, denoted ext, is the outside region and is filled with a homogeneous exterior medium, and its real permittivity is denoted ϵ_{ext} . The present method requires that we introduce three areas defined by two circular cylinders with directrix C_{min} and C_{max} . The directrix C_{min} is the inscribed circle of the directrix of surface (S), and C_{max} is the circumscribed circle (see Fig. 1). The area included between both circular cylinders is called the modulated area. Inside this area the permittivity is described by a 2π periodic with respect to θ tensor $\overline{\overline{\epsilon}}(r, \theta)$. Unless defined otherwise, both lower-case and capital letters in bold represent vectors.

An incident plane wave with wave vector \mathbf{k}_{ext} with transverse component $\mathbf{k}_{t,ext}$ and z component γ_0 falls on the device (Fig. 3). We introduce two angles: $\theta_{inc} = (-\mathbf{e}_x, \mathbf{k}_{t,ext})$ and $\varphi = (\mathbf{k}_{t,ext}, \mathbf{k}_{ext}) \in [-\pi/2, \pi/2]$. We as-

sume that the plane-wave components have a harmonic $\exp(-i\omega t)$ time dependence. Thus the incident vector field of \mathbf{E} and \mathbf{H} reads

$$\begin{cases} \mathbf{E}^{(inc)}(r, \theta, z, t) = \mathbf{A}_e \exp[i(\gamma_0 z - \omega t)] \\ \quad \times \exp[ik_{t,ext} r \cos(\theta - \theta_{inc} - \pi)] \\ \mathbf{H}^{(inc)}(r, \theta, z, t) = \mathbf{A}_h \exp[i(\gamma_0 z - \omega t)] \\ \quad \times \exp[ik_{t,ext} r \cos(\theta - \theta_{inc} - \pi)] \end{cases}, \quad (1)$$

in which $\omega = 2\pi/\lambda_0 \sqrt{\mu_0 \epsilon_0}$, $\gamma_0 = -k_{ext} \sin(\varphi)$, $k_{t,ext} = \sqrt{k_{ext}^2 - \gamma_0^2}$ with $k_{ext} = (2\pi/\lambda_0) \sqrt{\epsilon_{ext}/\epsilon_0}$ where λ_0 is the wavelength in vacuum. Moreover, the polarization of the incident electric field is defined by the azimuthal angle ϕ contained in the plane perpendicular to the wave vector \mathbf{k}_{ext} and with basic vectors $(\mathbf{p}_1, \mathbf{p}_2)$ [\mathbf{p}_1 is chosen to be included in the plane $(\mathbf{k}_{ext}, \mathbf{e}_z)$, see Fig. 4]. The relation between the $\mathbf{E}^{(inc)}$ amplitude noted as \mathbf{A}_e and the $\mathbf{H}^{(inc)}$ amplitude noted as \mathbf{A}_h with the incident wave vector reads thanks to the Maxwell equations in homogeneous regions:

$$\begin{cases} \mathbf{A}_e = [\cos(\phi)\mathbf{p}_1 + \sin(\phi)\mathbf{p}_2]|\mathbf{E}^{(inc)}| \\ \mathbf{A}_h = -\frac{1}{Z} \frac{\mathbf{k}_{ext}}{|\mathbf{k}_{ext}|} \times \mathbf{A}_e \end{cases} \quad \text{with } Z = \frac{1}{n_{ext}} \sqrt{\frac{\mu_0}{\epsilon_0}}, \quad (2)$$

in which $|\mathbf{E}^{(inc)}|$ and $|\mathbf{k}_{ext}|$ are the norms of their respective vectors $\mathbf{E}^{(inc)}$ and \mathbf{k}_{ext} . If the permittivity is a complex number, the cut of the square root $n_{ext} = \sqrt{\epsilon_{ext}}$ is then chosen as the second bisector as explained in Ref. 6. The total field has the same time dependence as the incident wave, and the invariance of the device with respect to z leads to an $\exp(i\gamma_0 z)$ dependence. Moreover, the cylindrical coordi-

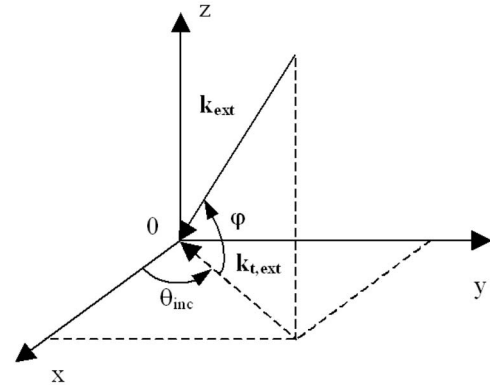


Fig. 3. Incident wave vector in the exterior homogeneous region and notations.

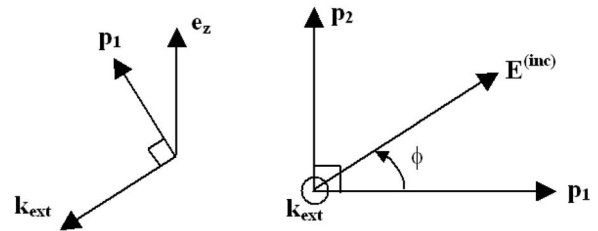


Fig. 4. Definitions and notations for the azimuthal angle ϕ of the incident electric field (\mathbf{p}_1 belongs to the plane defined by \mathbf{e}_z and \mathbf{k}_{ext}).

nate system naturally implies a 2π periodicity with respect to θ . In view of a numerical implementation of the theory, an electromagnetic and geometric quantity $u(r, \theta, z, t)$ will be represented by its Fourier series truncated to the N th order:

$$u(r, \theta, z, t) = \exp[i(\gamma_0 z - \omega t)] \sum_{n=-N}^{+N} u_n(r) \exp(in\theta) \text{ with } u_n(r) = \frac{1}{2\pi} \int_0^{2\pi} u(r, \theta) \exp[-in\theta] d\theta. \quad (3)$$

3. FAST FOURIER FACTORIZATION METHOD IN CYLINDRICAL COORDINATES EXTENDED TO A CONICAL MOUNTING

The aim of this work is to establish, in cylindrical coordinates, a set of equations satisfied by the electromagnetic field suitable for numerical computations. We make use of the recent progress in grating theory published under the name of fast Fourier factorization (FFF), but the case of cylindrical coordinates is not treated in the book describing the method.⁴ The FFF method starts from the classical differential method⁷ with efficient improvements in the factorizations rule concerning Fourier developments. In fact, we have to consider new factorization rules that take into account the Fourier truncation of developments and the discontinuities of any optogeometric quantities (across the diffracting surface). One of the key steps of the FFF method is to find the correct formulation in the Fourier space of the product between $\bar{\epsilon}$ and \mathbf{E} in the constitutive relation that must be injected into the Maxwell equations. Doing so, the Maxwell equations are restated in the Fourier space to obtain a set of coupled linear ordinary differential equations.

A. Formulation of the Linear Relation between \mathbf{E} and \mathbf{D} in a Truncated Fourier Space

1. Factorization Rules

As has been already treated in the paper concerning TM polarization,⁵ the FFF method consists in finding the best formulation in a truncated Fourier space of the product between the tensor $\bar{\epsilon}(r, \theta)$ and \mathbf{E} in the modulated region when we want to calculate \mathbf{D} given by

$$\mathbf{D} = \bar{\epsilon}(\mathbf{r}, \theta) \mathbf{E}. \quad (4)$$

In fact, the function $\bar{\epsilon}(r, \theta)$ is discontinuous across the surface (S). The mathematical basis of the FFF method was established by Li⁸ with factorization rules that allow one to obtain a solution of this problem. The first rule states that the Fourier components \tilde{h}_n of the product $\tilde{h}(x)$ of two periodic, piecewise-smooth bounded functions $\tilde{f}(x)$ and $\tilde{g}(x)$ that are not discontinuous at the same value of x are given by Laurent's rule:

$$\tilde{h}_n = (\tilde{f}\tilde{g})_n = \sum_{m=-N}^{+N} \tilde{f}_{n-m} \tilde{g}_m. \quad (5)$$

To simplify the equations that follow, we introduce the Toeplitz matrix $[\tilde{f}]$ defined by $([\tilde{f}])_{n,m} = \tilde{f}_{n-m}$ and the col-

umn vector $[\tilde{g}]$ with elements \tilde{g}_m . Thus the last equation reads in matrix notation:

$$[\tilde{f}\tilde{g}] = [\tilde{f}][\tilde{g}]. \quad (6)$$

The second rule given by Li⁸ states that a product of two piecewise-smooth, bounded periodic functions that have only pairwise-complementary jump discontinuities (i.e., that have a continuous product) cannot be factorized by Laurent's rule, but it can be factorized by the inverse rule:

$$[\tilde{f}\tilde{g}]_n = \sum_{m=-N}^{+N} \left(\left[\begin{array}{c} 1 \\ \tilde{f} \end{array} \right]^{-1} \right)_{n,m} \tilde{g}_m. \quad (7)$$

Or in matrix notation,

$$[\tilde{f}\tilde{g}] = \left[\begin{array}{c} 1 \\ \tilde{f} \end{array} \right]^{-1} [\tilde{g}]. \quad (8)$$

Finally, the most general situation concerns a product of two piecewise-smooth, bounded periodic functions that have discontinuities at the same value of x with non-complementary jump discontinuities. Such a product can be correctly factorized neither by Laurent's rule nor by the inverse rule. This last case occurs in Eq. (4).

2. Intermediate Notations

The basic idea of the FFF method is to use the first two rules to write a new formulation of Eq. (4), thanks to a suitable continuation of the concept of normal vector. We consider at each point of the surface (S) the normal vector of (S) noted as \mathbf{N} whose components are N_r, N_θ, N_z , and two orthogonal tangential vectors of (S) denoted \mathbf{T}_1 with components $(T_{1r}, T_{1\theta}, T_{1z})$ and \mathbf{T}_2 with components $(T_{2r}, T_{2\theta}, T_{2z})$ such that $\mathbf{N} = \mathbf{T}_2 \times \mathbf{T}_1$ (see Fig. 5). The projections of the fields \mathbf{E} and \mathbf{D} on \mathbf{T}_1 , \mathbf{N} , and \mathbf{T}_2 define three field components continuous across the surface (S): \mathbf{E}_{T_1} , \mathbf{D}_N , and \mathbf{E}_{T_2} ; they permit us to create a column denoted \mathbf{F}_ϵ respectively made with these components, whose size is $3(2N+1)$. If we define a generalization of the scalar product applied to a vector $\tilde{\mathbf{v}}$ and a matrix \mathbf{P} by

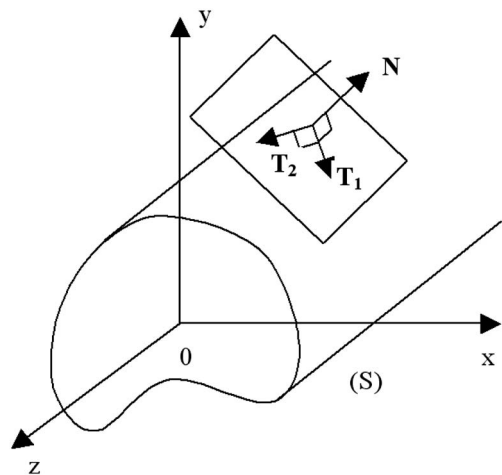


Fig. 5. Tangential and normal vectors of a cylindrical object.

$$\mathbf{v} \cdot \mathbf{P} = \begin{bmatrix} v_r \\ v_\theta \\ v_z \end{bmatrix} \cdot \begin{bmatrix} P_{rr} & P_{r\theta} & P_{rz} \\ P_{\theta r} & P_{\theta\theta} & P_{\theta z} \\ P_{zr} & P_{z\theta} & P_{zz} \end{bmatrix} = \begin{bmatrix} v_r P_{rr} + v_\theta P_{\theta r} + v_z P_{zr} \\ v_r P_{r\theta} + v_\theta P_{\theta\theta} + v_z P_{z\theta} \\ v_r P_{rz} + v_\theta P_{\theta z} + v_z P_{zz} \end{bmatrix}, \quad (9)$$

we obtain

$$\mathbf{F}_\epsilon = O_\epsilon \mathbf{E} \quad (10)$$

with

$$O_\epsilon = \begin{bmatrix} T_{1r} & T_{1\theta} & T_{1z} \\ (\mathbf{N} \cdot \bar{\epsilon})_r & (\mathbf{N} \cdot \bar{\epsilon})_\theta & (\mathbf{N} \cdot \bar{\epsilon})_z \\ T_{2r} & T_{2\theta} & T_{2z} \end{bmatrix}. \quad (11)$$

Thus for the electric field we can write $\mathbf{E} = C_\epsilon \mathbf{F}_\epsilon$ with $C_\epsilon = O_\epsilon^{-1}$. Tedious algebraic calculations lead to

$$C_\epsilon = \frac{1}{\mathbf{N} \cdot \bar{\epsilon} \cdot \mathbf{N}} \begin{bmatrix} ((\mathbf{N} \cdot \bar{\epsilon}) \wedge \mathbf{T}_2)_r & N_r & -((\mathbf{N} \cdot \bar{\epsilon}) \wedge \mathbf{T}_1)_r \\ ((\mathbf{N} \cdot \bar{\epsilon}) \wedge \mathbf{T}_2)_\theta & N_\theta & -((\mathbf{N} \cdot \bar{\epsilon}) \wedge \mathbf{T}_1)_\theta \\ ((\mathbf{N} \cdot \bar{\epsilon}) \wedge \mathbf{T}_2)_z & N_z & -((\mathbf{N} \cdot \bar{\epsilon}) \wedge \mathbf{T}_1)_z \end{bmatrix}. \quad (12)$$

Then $\mathbf{D} = \bar{\epsilon} \mathbf{E} = \bar{\epsilon} C_\epsilon \mathbf{F}_\epsilon$, and finally,

$$\mathbf{D} = \bar{\epsilon} C_\epsilon O_\epsilon \mathbf{E}. \quad (13)$$

3. New Relation between $[\mathbf{D}]$ and $[\mathbf{E}]$

We will write this last equation in the truncated Fourier space using the factorization rules mentioned above. Since $\bar{\epsilon} C_\epsilon$ is discontinuous and \mathbf{F}_ϵ is continuous, we apply Laurent's rule for these two factors. Introducing the column $[\mathbf{D}]$ made of three blocks $[D_r]$, $[D_\theta]$, and $[D_z]$, each block containing the Fourier coefficients of the corresponding vector component, we write $[\mathbf{D}] = \llbracket \bar{\epsilon} C_\epsilon \rrbracket [\mathbf{F}_\epsilon]$. Then the inverse rule is used since $\mathbf{F}_\epsilon = O_\epsilon \mathbf{E}$ is continuous while O_ϵ and \mathbf{E} are discontinuous: $[O_\epsilon \mathbf{E}] = \llbracket O_\epsilon^{-1} \rrbracket^{-1} [\mathbf{E}] = \llbracket C_\epsilon \rrbracket^{-1} [\mathbf{E}]$. Finally, we find

$$[\mathbf{D}] = Q_\epsilon(\mathbf{r}) [\mathbf{E}], \quad (14)$$

with

$$Q_\epsilon(r) = \llbracket \bar{\epsilon} C_\epsilon \rrbracket \llbracket C_\epsilon \rrbracket^{-1}. \quad (15)$$

B. Maxwell Equations in a Truncated Fourier Space

Differentiating the series in Eq. (3) with respect to θ results in multiplying the n th term by "in". Thus introducing a diagonal matrix α such that $(\alpha)_{nm} = n \delta_{nm}$, the derivation reads in matrix notation as

$$\frac{\partial [U]}{\partial \theta} = i\alpha [U]. \quad (16)$$

According to the z and t dependence of the total fields, the Maxwell equations written in the cylindrical coordinate system become

$$\frac{1}{r} \alpha [E_z] - \gamma_0 [E_\theta] - \omega [B_r] = 0, \quad (17)$$

$$i\gamma_0 [E_r] - \frac{d[E_z]}{dr} - i\omega [B_\theta] = 0, \quad (18)$$

$$\frac{1}{r} \left([E_\theta] + r \frac{d[E_\theta]}{dr} - i\alpha [E_r] \right) - i\omega [B_z] = 0, \quad (19)$$

$$\frac{1}{r} \alpha [H_z] - \gamma_0 [H_\theta] + \omega [D_r] = 0, \quad (20)$$

$$i\gamma_0 [H_r] - \frac{d[H_z]}{dr} + i\omega [D_\theta] = 0, \quad (21)$$

$$\frac{1}{r} \left([H_\theta] + r \frac{d[H_\theta]}{dr} - i\alpha [H_r] \right) + i\omega [D_z] = 0. \quad (22)$$

From Eq. (14) we obtain the expression of each block of $[\mathbf{D}]$ in the cylindrical coordinate system in terms of the \mathbf{E} blocks. We introduce the following notation for the Q_ϵ matrix:

$$Q_\epsilon = \begin{bmatrix} Q_{\epsilon,rr} & Q_{\epsilon,r\theta} & Q_{\epsilon,rz} \\ Q_{\epsilon,\theta r} & Q_{\epsilon,\theta\theta} & Q_{\epsilon,\theta z} \\ Q_{\epsilon,zr} & Q_{\epsilon,z\theta} & Q_{\epsilon,zz} \end{bmatrix}. \quad (23)$$

Equation (20) leads to

$$[E_r(r)] = Q_{\epsilon,rr}^{-1} \left(\frac{\gamma_0}{\omega} [H_\theta(r)] - \frac{\alpha}{r\omega} [H_z(r)] - Q_{\epsilon,r\theta} [E_\theta(r)] - Q_{\epsilon,rz} [E_z(r)] \right), \quad (24)$$

and Eq. (17) becomes

$$[H_r(r)] = \frac{1}{\mu_0 \omega} \left(\frac{\alpha}{r} [E_z(r)] - \gamma_0 [E_\theta(r)] \right). \quad (25)$$

These two last equations and Eq. (23) permit us to rewrite Eqs. (18), (19), (21), and (22). Finally, we obtain a set of first-order differential equations written in a four-block matrix form:

$$\frac{d}{dr} \begin{bmatrix} [E_\theta] \\ [E_z] \\ [H_\theta] \\ [H_z] \end{bmatrix} = iM(r) \begin{bmatrix} [E_\theta] \\ [E_z] \\ [H_\theta] \\ [H_z] \end{bmatrix}, \quad (26)$$

with

$$M(r) = \begin{bmatrix} -\frac{1}{r}\alpha Q_{\epsilon,rr}^{-1}Q_{\epsilon,r\theta} + \frac{i}{r}I_d & -\frac{1}{r}\alpha Q_{\epsilon,rr}^{-1}Q_{\epsilon,rz} & \frac{\gamma_0}{\omega r}\alpha Q_{\epsilon,rr}^{-1} & \omega\mu_0 I_d - \frac{\alpha}{\omega r^2}Q_{\epsilon,rr}^{-1}\alpha \\ -\gamma_0 Q_{\epsilon,rr}^{-1}Q_{\epsilon,r\theta} & -\gamma_0 Q_{\epsilon,rr}^{-1}Q_{\epsilon,rz} & \frac{\gamma_0^2}{\omega}Q_{\epsilon,rr}^{-1} - \omega\mu_0 I_d & -\frac{\gamma_0}{r\omega}Q_{\epsilon,rr}^{-1}\alpha \\ \omega(Q_{\epsilon,zr}Q_{\epsilon,rr}^{-1}Q_{\epsilon,r\theta} - Q_{\epsilon,z\theta}) - \frac{\gamma_0}{\mu_0\omega r}\alpha & \frac{\alpha^2}{\omega\mu_0 r^2} + \omega(Q_{\epsilon,zr}Q_{\epsilon,rr}^{-1}Q_{\epsilon,rz} - Q_{\epsilon,zz}) & \frac{i}{r}I_d - \gamma_0 Q_{\epsilon,zr}Q_{\epsilon,rr}^{-1} & Q_{\epsilon,zr}Q_{\epsilon,rr}^{-1}\frac{\alpha}{r} \\ \omega(Q_{\epsilon,\theta\theta} - Q_{\epsilon,\theta r}Q_{\epsilon,rr}^{-1}Q_{\epsilon,r\theta}) - \frac{\gamma_0^2}{\mu_0\omega}I_d & \frac{\gamma_0}{\mu_0\omega r}\alpha + \omega(Q_{\epsilon,\theta z} - Q_{\epsilon,\theta r}Q_{\epsilon,rr}^{-1}Q_{\epsilon,rz}) & Q_{\epsilon,\theta r}Q_{\epsilon,rr}^{-1}\gamma_0 & -Q_{\epsilon,\theta r}Q_{\epsilon,rr}^{-1}\frac{\alpha}{r} \end{bmatrix}, \tag{27}$$

where I_d is the identity matrix. It is important to notice that the $M(r)$ matrix depends only on the r coordinate and that its size is $4(2N+1) \times 4(2N+1)$. In brief, Eq. (26) is a new formulation of the Maxwell equations in cylindrical coordinates in a truncated Fourier space, which is valid in any lossless or lossy, anisotropic and/or inhomogeneous medium.

4. RESOLUTION OF THE DIFFRACTION PROBLEM IN THE CASE OF AN ISOTROPIC AND HOMOGENEOUS MEDIUM

The resolution of the diffraction problem is much simpler if the diffracting object is made of an isotropic and homogeneous material, since the field in such a region can then be expressed in terms of Bessel functions. Thus, from now on, we consider that the region (int) is filled with an isotropic and homogeneous medium. Its permittivity tensor is reduced to a complex number ϵ_{int} (see Fig. 1).

A. Linear Relation between E and D in the Case of an Isotropic Medium

In the present case, the tensor $\bar{\epsilon}$ in Eq. (4) (defined in the modulated area) becomes a function $\epsilon(r, \theta)$. So we have $\mathbf{N} \cdot \bar{\epsilon} \cdot \mathbf{N} = \epsilon(r, \theta)(\mathbf{N} \cdot I_d) \cdot \mathbf{N} = \epsilon(r, \theta)$. Moreover, $(\mathbf{N} \cdot \bar{\epsilon}) \wedge \mathbf{T}_2 = \epsilon(r, \theta)\mathbf{N} \wedge \mathbf{T}_2 = \epsilon(r, \theta)\mathbf{T}_1$ and $(\mathbf{N} \cdot \bar{\epsilon}) \wedge \mathbf{T}_1 = \epsilon(r, \theta)\mathbf{N} \wedge \mathbf{T}_1 = -\epsilon(r, \theta)\mathbf{T}_2$. Thus the term $\bar{\epsilon}C_\epsilon$ reduces to

$$\begin{bmatrix} \epsilon N_\theta & N_r & 0 \\ -\epsilon N_r & N_\theta & 0 \\ 0 & 0 & 1 \end{bmatrix}.$$

Considering $\tilde{f}(x)$ and $\tilde{g}(x)$ as 2π periodic functions discontinuous at different values of x and using the first factorization rule, we obtain the following results: $[\tilde{f}\tilde{g}] = [\tilde{f}][\tilde{g}]$. By the use of this property into the Toeplitz matrices $[[C_\epsilon]]$ and $[[\epsilon C_\epsilon]]$ in Eq. (14), we obtain the same formula as in the work on the TM case⁵:

Q_ϵ

$$= \begin{bmatrix} [[\epsilon][N_\theta^2]] + \left[\left[\frac{1}{\epsilon}\right]\right]^{-1} [[N_r^2]] & -\left([[\epsilon]] - \left[\left[\frac{1}{\epsilon}\right]\right]^{-1}\right) [[N_r N_\theta]] & 0 \\ -\left([[\epsilon]] - \left[\left[\frac{1}{\epsilon}\right]\right]^{-1}\right) [[N_r N_\theta]] & [[\epsilon][N_r^2]] + \left[\left[\frac{1}{\epsilon}\right]\right]^{-1} [[N_\theta^2]] & 0 \\ 0 & 0 & [[\epsilon]] \end{bmatrix}. \tag{28}$$

Since $[\mathbf{D}]$ and $[\mathbf{E}]$ have dimension $3(2N+1)$, the size of this matrix is $3(2N+1) \times 3(2N+1)$. Moreover, we notice that the matrix Q_ϵ contains the Toeplitz matrices $[[N_r^2]]$, $[[N_\theta^2]]$, and $[[N_r N_\theta]]$. But N_r and N_θ are defined only on the surface (S); that is why we need to extend their definition inside the whole modulated area. The extension can be done in different ways. If the surface is well defined along the interval $[0, 2\pi]$ of θ (g is continuous on $[0, 2\pi]$), the unit vector normal to the surface (S) can read as

$$\mathbf{N}[r = g(\theta), \theta] = \frac{\mathbf{grad}(f)}{|\mathbf{grad}(f)|} \Bigg|_{r=g(\theta)} \quad \text{with } f(r, \theta) = r - g(\theta) = 0. \tag{29}$$

From its definition, \mathbf{N} depends only on θ and is defined on (S) only. But we extend its definition to the entire modulated area ($R_{\min} < r < R_{\max}$) by introducing a new vector continuous across the diffracting surface (S) and defined by

$$\forall r \in [R_{\min}, R_{\max}], \quad \mathbf{N}(r, \theta) = \frac{\mathbf{grad}(f)}{|\mathbf{grad}(f)|} \Bigg|_{r=g(\theta)}. \tag{30}$$

A second way to extend the normal vector consists in considering only the value of \mathbf{N} at the intersection points between the surface (S) and the circle in the cross section of radius r , and taking an arbitrary vector elsewhere, providing that we avoid discontinuities and strong variations to avoid the Gibbs phenomenon. The main disadvantage of the second method is the longer needed computation time related to the fact that the normal vector now depends on r and θ , which requires computing the Fourier coefficients of its three components at any integration

step that will occur in the numerical resolution of the boundary-value problem.

B. Field Expressions in the Homogeneous Regions

According to the r dependence of the $M(r)$ matrix, no explicit expression of the field in the modulated area can be found. On the other hand, the Maxwell equations in the homogeneous regions (j =int or ext) permit us to obtain a set of independent second-order differential equations governing the Fourier coefficients of the z component of the magnetic and electric field $G_{z,n}$ depending on $k_{t,j}r$:

$$(k_{t,j}r)^2 \frac{d^2 G_{z,n}}{d(k_{t,j}r)^2} + k_{t,j}r \frac{dG_{z,n}}{d(k_{t,j}r)} + [(k_{t,j}r)^2 - n^2]G_{z,n} = 0$$

with $G_{z,n} \in \{E_{z,n}, H_{z,n}\}$, (31)

the solutions of which are

$$H_{z,n} = A_{h,n}^{(j)} J_n(k_{t,j}r) + B_{h,n}^{(j)} H_n^+(k_{t,j}r),$$

$$E_{z,n} = A_{e,n}^{(j)} J_n(k_{t,j}r) + B_{e,n}^{(j)} H_n^+(k_{t,j}r). \quad (32)$$

with $k_{t,j}^2 = k_j^2 - \gamma_0^2$ and $k_j^2 = \omega^2 \mu_0 \epsilon_j$. The others components of the field are given by

$$H_r = \frac{1}{k_{t,j}^2} \left(i \gamma_0 \frac{\partial H_z}{\partial r} - \frac{i \omega \epsilon_j}{r} \frac{\partial E_z}{\partial \theta} \right),$$

$$H_\theta = \frac{1}{k_{t,j}^2} \left(\frac{i \gamma_0}{r} \frac{\partial H_z}{\partial \theta} + i \omega \epsilon_j \frac{\partial E_z}{\partial r} \right),$$

$$E_r = \frac{1}{k_{t,j}^2} \left(i \gamma_0 \frac{\partial E_z}{\partial r} + \frac{i \omega \mu_0}{r} \frac{\partial H_z}{\partial \theta} \right),$$

$$E_\theta = \frac{1}{k_{t,j}^2} \left(\frac{i \gamma_0}{r} \frac{\partial E_z}{\partial \theta} - i \omega \mu_0 \frac{\partial H_z}{\partial r} \right). \quad (33)$$

Equations (32) and (33), which allow us to find the components of the field developments, can be written in a matrix form. Thus we define a matrix $\Psi^{(j)}(r)$ made of 4×4 blocks, each block size being $(2N+1)$. This matrix links the vector $[F(r)]$ containing the components of successively E_θ , E_z , H_θ , and H_z with the vector $[V^{(j)}(r)]$ containing the components $A_{e,n}^{(j)} J_n(k_{t,j}r)$, $A_{h,n}^{(j)} J_n(k_{t,j}r)$, $B_{e,n}^{(j)} H_n^+(k_{t,j}r)$, and $B_{h,n}^{(j)} H_n^+(k_{t,j}r)$ by

$$[F(r)] = \Psi^{(j)}(r) [V^{(j)}(r)] \text{ with } \Psi^{(j)}(r) = \begin{bmatrix} \frac{1}{r} p^{(j)} & q^{(j)} & \frac{1}{r} p^{(j)} & q^{(j)} \\ I_d & 0 & I_d & 0 \\ -\frac{\epsilon_j}{\mu_0} q^{(j)} & \frac{1}{r} p^{(j)} & -\frac{\epsilon_j}{\mu_0} q^{(j)} & \frac{1}{r} p^{(j)} \\ 0 & I_d & 0 & I_d \end{bmatrix}, \quad (34)$$

in which

$$(p^{(j)})_{nm} = -\frac{\gamma_0}{k_{t,j}^2} n \delta_{nm}, \quad (35)$$

$$(q_e^{(j)})_{nm} = -\frac{i \omega \mu_0}{k_{t,j}^2} \left(\frac{n}{r} - k_{t,j} \frac{J_{n+1}(k_{t,j}r)}{J_n(k_{t,j}r)} \right) \delta_{nm}, \quad (36)$$

$$(q_h^{(j)})_{nm} = -\frac{i \omega \mu_0}{k_{t,j}^2} \left(\frac{n}{r} - k_{t,j} \frac{H_{n+1}^+(k_{t,j}r)}{H_n^+(k_{t,j}r)} \right) \delta_{nm}. \quad (37)$$

We notice that the size of vectors $[F(r)]$ and $[V^{(j)}(r)]$ is $4(2N+1)$.

C. Integration of the Differential Set with the S-matrix Propagation Algorithm

A basic integration with a shooting method through the modulus area gives the transmission matrix T of the diffracting device. However, the T matrix may be ill-conditioned because of numerical contaminations. Important index gap or strong growth of the function $f(r, \theta)$ increases such numerical contaminations. To improve the convergence of the results, the S -matrix propagation algorithm is used.^{4,9} In this subsection, this algorithm is presented in a matrix formulation. The modulated area is divided into L slices of which the circular boundary cylinders have radius r_s , $s \in [1, L+1]$ ($r_1 = R_{\min}$ and $r_{L+1} = R_{\max}$). We introduce a infinitely thin homogeneous layer with a permittivity of ϵ_{ext} between each slice except at R_{\min} (see Fig. 6). The resolution of the diffraction problem uses a shooting method that consists of turning the boundary-value problem into an initial-value problem. At the s th slice, we take $4(2N+1)$ independent initial column vectors noted as $[V_p]$: $([V_p])_i = \delta_{pi}$ with $i \in [1, 4(2N+1)]$. In what follows, the sign \wedge will denote a matrix, used in the integration process, built from a list of column vectors. These columns form the identity matrix

$$\hat{V}(r_s) = (\dots, [V_p], \dots) = I_d, \quad (38)$$

and the corresponding fields read $\hat{F}(r_s) = \Psi^{(\text{ext})}(r_s) I_d = \Psi^{(\text{ext})}(r_s)$ at r_s [if $s=1$ we take $\Psi^{(\text{int})}(r_1)$]. The matrix $\hat{F}(r_s)$

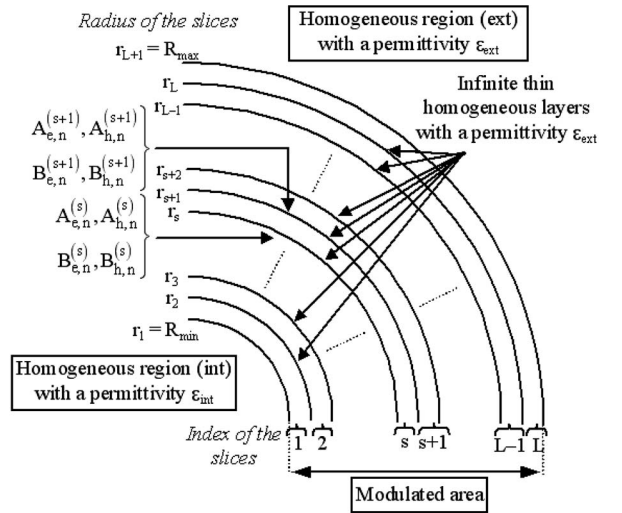


Fig. 6. Notations of the splitting of the modulated area for the S -propagation algorithm (the coefficients $A_{f,n}^{(s)}$ and $B_{f,n}^{(s)}$ with $f=e$ or h are amplitudes of the field in the infinite thin homogeneous layer at $r=r_s$).

contains the column vectors $([F(r_s)])_i$ with $i \in [1, 4(2N + 1)]$, used as initial values of the field, and we integrate the differential set of Eq. (26) using a suitable algorithm (combining Runge–Kutta and Adams–Moulton algorithms). Compared with Ref. 3, the notations of the $\Psi^{(j)}$ matrix are changed [see Eqs. (31) and (42) in Ref. 3]: The $\Psi^{(j)}$ matrices are normalized by the Bessel and the Hankel functions so as to inject well-conditioned matrices as an initial value in the integration process. This new notation induces that the vector $[V^{(j)}]$ contains the Bessel and the Hankel functions. At the end of the integration, the result is a matrix noted as $\hat{F}_{\text{integ}}(r_{s+1})$ giving the field at r_{s+1} , from which we derived from Eq. (34) the matrix

$$\hat{V}(r_{s+1}) = \{\Psi^{(\text{ext})}(r_{s+1})\}^{-1} \hat{F}_{\text{integ}}(r_{s+1});$$

using Eq. (38), we obtain

$$\hat{V}(r_{s+1}) = \{\Psi^{(\text{ext})}(r_{s+1})\}^{-1} \hat{F}_{\text{integ}}(r_{s+1}) \hat{V}(r_s).$$

This last equation shows that the transmission matrix $T^{(s)}$ that links the coefficients of the developments of the field at r_s to the coefficients of the development of the field at r_{s+1} is given by

$$T^{(s)} = \{\Psi^{(\text{ext})}(r_{s+1})\}^{-1} \hat{F}_{\text{integ}}(r_{s+1}). \quad (39)$$

The integration through each slice provides a $T^{(s)}$ matrix that links the field at r_{s+1} to the field at r_s . From this matrix, we deduce a $S^{(s)}$ matrix that links the fields at r_s and r_1 , defined by

$$\forall s \in [1, L + 1], \quad \begin{bmatrix} \vdots \\ B_{e,n}^{(s)} H_n^+(k_{t,\text{ext}} r_s) \\ \vdots \\ B_{h,n}^{(s)} H_n^+(k_{t,\text{ext}} r_s) \\ \vdots \\ A_{e,n}^{(1)} J_n(k_{t,\text{int}} r_1) \\ \vdots \\ A_{h,n}^{(1)} J_n(k_{t,\text{int}} r_1) \\ \vdots \\ \vdots \\ B_{e,n}^{(1)} H_n^+(k_{t,\text{int}} r_1) \\ \vdots \\ B_{h,n}^{(1)} H_n^+(k_{t,\text{int}} r_1) \\ \vdots \\ A_{e,n}^{(s)} J_n(k_{t,\text{ext}} r_s) \\ \vdots \\ A_{h,n}^{(s)} J_n(k_{t,\text{ext}} r_s) \\ \vdots \end{bmatrix} = \begin{bmatrix} S_{11}^{(s)} & S_{12}^{(s)} \\ S_{21}^{(s)} & S_{22}^{(s)} \end{bmatrix} \begin{bmatrix} \vdots \\ A_{e,z} i^n \exp(-in\theta_{\text{inc}}) \\ \vdots \\ A_{h,z} i^n \exp(-in\theta_{\text{inc}}) \\ \vdots \\ \vdots \\ B_{e,n}^{(\text{ext})} \\ \vdots \\ B_{h,n}^{(\text{ext})} \\ \vdots \\ \vdots \end{bmatrix}. \quad (40)$$

Here the index (s) of the amplitudes $A_{e,n}^{(s)}$, $A_{h,n}^{(s)}$, $B_{e,n}^{(s)}$, and $B_{h,n}^{(s)}$ can be replaced by (int) when $s=1$ and (ext) when $s=L+1$. For the particular case of $s=1$, the $S^{(s)}$ matrix becomes the identical matrix and $k_{t,\text{ext}}$ becomes equal to

$k_{t,\text{int}}$. We have checked that all blocks of this matrix are well conditioned (see also Ref. 4). Briefly, the $T^{(s)}$ matrix links the fields at layer (s) and the fields at layer $(s+1)$ while the $S^{(s)}$ matrix links the scattered fields and the incident fields. The $S^{(s)}$ matrix blocks of the $(s+1)$ th interface are expressed according to those of the s th interface and to the $T^{(s)}$ matrix blocks $T_{mn}^{(s)}$ of the s th slice:

$$\begin{aligned} S_{22}^{(s+1)} &= S_{22}^{(s)} [T_{11}^{(s)} + T_{12}^{(s)} S_{12}^{(s)}]^{-1}, \\ S_{12}^{(s+1)} &= [T_{21}^{(s)} + T_{22}^{(s)} S_{12}^{(s)}] [T_{11}^{(s)} + T_{12}^{(s)} S_{12}^{(s)}]^{-1}, \\ S_{21}^{(s+1)} &= S_{21}^{(s)} - S_{22}^{(s+1)} T_{12}^{(s)} S_{11}^{(s)}, \\ S_{11}^{(s+1)} &= T_{22}^{(s)} S_{11}^{(s)} - S_{12}^{(s+1)} T_{12}^{(s)} S_{11}^{(s)}. \end{aligned} \quad (41)$$

At the end of the integration across the modulated area, we obtain the S matrix of the whole scattering device, which depends only on the surface (S) and on the optical parameters of the media. This matrix links the diffracted field at R_{max} and R_{min} to the incident field at R_{max} and R_{min} . In fact, expressing the exponential function in Eq. (1) in terms of Bessel functions,¹⁰ the incident field can be defined in the form

$$\begin{cases} H_z^{(\text{inc})} = \exp(i\gamma_0 z) \sum_{n=-\infty}^{+\infty} A_{h,z} \exp(-in\theta_{\text{inc}}) i^n J_n(k_{t,\text{ext}} r) \exp(in\theta) \\ E_z^{(\text{inc})} = \exp(i\gamma_0 z) \sum_{n=-\infty}^{+\infty} A_{e,z} \exp(-in\theta_{\text{inc}}) i^n J_n(k_{t,\text{ext}} r) \exp(in\theta) \end{cases}. \quad (42)$$

Inside the internal region containing the origin of coordinates, we must state $B_{e,n}^{(\text{int})} = B_{h,n}^{(\text{int})} = 0 \forall n$ to avoid a divergence of the field ($H_n^+(0) \rightarrow \infty \forall n$). This condition allows us to derive through Eq. (40)

$$\begin{bmatrix} \vdots \\ A_{e,n}^{(\text{int})} \\ \vdots \\ A_{h,n}^{(\text{int})} \\ \vdots \end{bmatrix} = S_{22} \begin{bmatrix} \vdots \\ A_{e,z} i^n \exp(-in\theta_{\text{inc}}) \\ \vdots \\ A_{h,z} i^n \exp(-in\theta_{\text{inc}}) \\ \vdots \end{bmatrix}, \quad \begin{bmatrix} \vdots \\ B_{e,n}^{(\text{ext})} \\ \vdots \\ B_{h,n}^{(\text{ext})} \\ \vdots \end{bmatrix} = S_{12} \begin{bmatrix} \vdots \\ A_{e,z} i^n \exp(-in\theta_{\text{inc}}) \\ \vdots \\ A_{h,z} i^n \exp(-in\theta_{\text{inc}}) \\ \vdots \end{bmatrix}. \quad (43)$$

5. NUMERICAL APPLICATION ON PARTICULAR CASES

A. First Validation Study

The present theory has been implemented using the FORTRAN programming language. It is worth noticing that the results of the TM and TE polarization studied

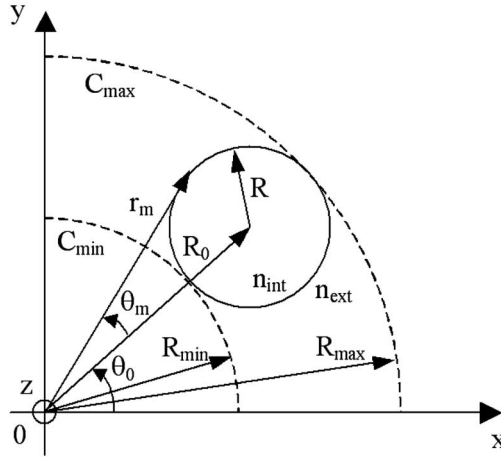


Fig. 7. Cross section of a circular cylinder centered outside the origin and filled with isotropic and homogeneous media with $R = 1 \mu\text{m}$, $R_0 = 2 \mu\text{m}$, $\theta_0 = 0^\circ$, $n_{\text{int}} = 1.6 + 0.2i$, and $n_{\text{ext}} = 1$, and notations.

previously⁵ are associated with the particular case of conical diffraction with $\gamma_0 = 0$. In this case, the current numerical implementation written for conical diffraction gives the same results as the ones computed previously in Ref. 5. To validate and illustrate in more detail the FFF method applied to cylindrical coordinates, we first study the simple case of one circular cylinder centered outside the origin with a radius R and the center with (R_0, θ_0) polar coordinates (see Fig. 7). The r coordinate defined on the circle and related to the maximal angle θ_m defined is noted as $r_m = \sqrt{R_0^2 - R^2}$. On the θ range where the circle is defined in the cross section ($[\theta_0 - \theta_m, \theta_0 + \theta_m]$), the diffracting surface directrix equation is given by

$$r(\theta) = R_0 \cos(\theta) \pm \sqrt{R^2 - R_0^2 \sin^2(\theta)},$$

$$\theta(r) = \cos^{-1}\left(\frac{r^2 + r_0^2 - R^2}{2r_0 r}\right), \quad (44)$$

where the $+$ sign is related to $r \in [R_0 - R, r_m]$ and the $-$ sign is related to $r \in [r_m, R_0 + R]$. In the modulated area, the permittivity is described by a step function $\epsilon(r, \theta)$ with respect to θ ; thus obtaining its Fourier development and the Toeplitz matrix $\llbracket \epsilon \rrbracket$ remains easy. The $N_\theta(\theta)$ function is given by

$$N_\theta(\theta) = \frac{r_0}{R} \sin(\theta - \theta_0). \quad (45)$$

We mention that the r component of the surface's normal vector is deduced by $N_r = \pm \sqrt{1 - N_\theta^2}$. Outside $[\theta_0 - \theta_m, \theta_0 + \theta_m]$ we could state that the N_θ^2 function is extended to unity. In this case, the N_θ^2 , N_r^2 , and $N_r N_\theta$ functions would have the advantages of the continuity and of the r independency. Since these functions would be r independent, their Toeplitz matrices would be calculated once before the integration process. However, it is interesting to point out that, along a circle with radius r included in the modulated area, the $N_\theta^2(r, \theta)$ is defined only by one or two points with the same $|N_\theta^2|$ value. Then we have chosen a straight extension of a $N_\theta^2(r, \theta)$ function with a constant

value of N_θ^2 evaluated at $\theta(r)$. The main advantage of such an extension is the simplicity of the calculation of its developments: $[N_\theta^2]_0 = N_\theta^2[\theta(r)]$ and $[N_\theta^2]_n = 0, \forall n \neq 0$. On the other hand, the $N_r N_\theta(r, \theta)$ function becomes discontinuous, which leaves the determination of its Fourier coefficients easy but increases the Gibbs phenomena. The numerical results show that the two extensions lead to similar convergence when the order of the Fourier developments is increased.

The differential cross section (DCS) that is determined with the asymptotic form of the Hankel functions of the diffracted field for $r \rightarrow \infty$ is given by

$$\sigma(\theta) = 2\pi \frac{k_0^2}{k_{t,\text{ext}}^2} \left[\left| \sqrt{\frac{2}{\pi k_{t,\text{ext}}}} \sum_{n=-\infty}^{+\infty} (-i)^n B_{e,n}^{(\text{ext})} e^{in\theta} \right|^2 + \frac{\mu_0}{\epsilon_{\text{ext}}} \left| \sqrt{\frac{2}{\pi k_{t,\text{ext}}}} \sum_{n=-\infty}^{+\infty} (-i)^n B_{h,n}^{(\text{ext})} e^{in\theta} \right|^2 \right]. \quad (46)$$

To validate our theory and its numerical implementation, we compare the FFF method results with the ones obtained with the MM.^{1,3} We study the scattering by a single cylinder (see Fig. 7) and compute the DCS with the two methods. Figure 8 shows the results of the DCS for $\lambda_0 = 1 \mu\text{m}$ and $\lambda_0 = 0.5 \mu\text{m}$ with a logarithmic scale for the Y axis; as can be seen, the FFF method results agree

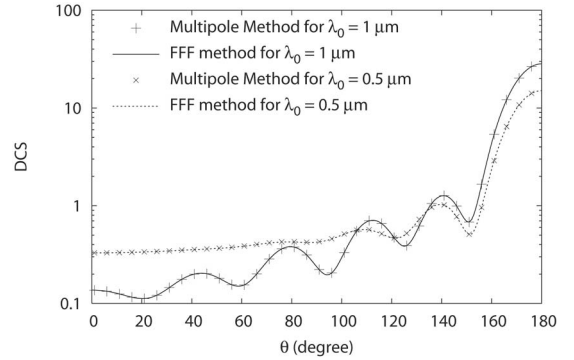


Fig. 8. DCS ($\theta = 0^\circ$ to 180°) for the circular cylinder in Fig. 7 with $\theta_{\text{inc}} = 0^\circ$, $\varphi = 30^\circ$, $\phi = 0^\circ$, and $N = 50$; comparison of the FFF method and MM for $\lambda_0 = 1 \mu\text{m}$ and $\lambda_0 = 0.5 \mu\text{m}$.

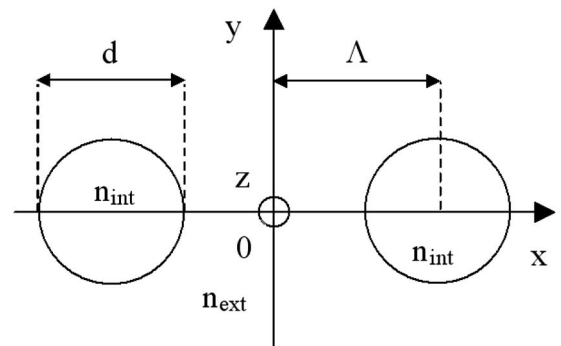


Fig. 9. Cross section of two identical circular cylinders on the X axis centered outside the origin with $d = 1 \mu\text{m}$, $\Lambda = 1.5 \mu\text{m}$, $n_{\text{int}} = 1.4$, and $n_{\text{ext}} = 1$.

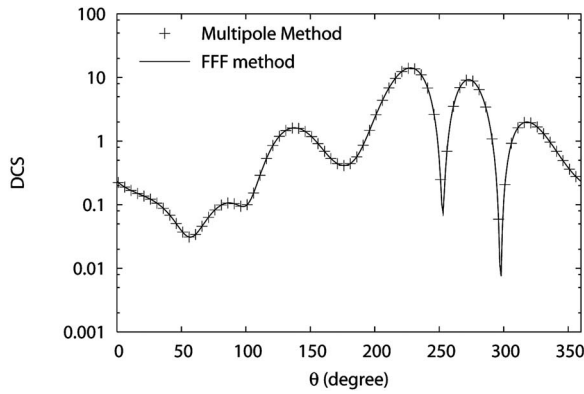


Fig. 10. DCS ($\theta=0^\circ$ to 360°) for the two identical circular cylinders on the X axis shown in Fig. 9 with $\lambda_0=2 \mu\text{m}$, $\theta_{\text{inc}}=45^\circ$, $\varphi=30^\circ$, $\phi=0^\circ$, and $N=60$; comparison between the FFF method and the MM.

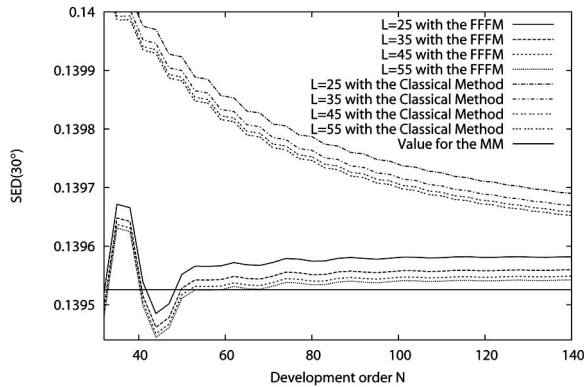


Fig. 11. Convergence test according to the order of the truncated Fourier series (N) of the point at 30° in the DCS of the FFF method (FFFM) (illustrated by Fig. 8) and of the classical differential method with $\lambda_0=1 \mu\text{m}$ and with different values of L (number of slices for the S algorithm) compared with the MM value.

fairly well with the MM ones. Then we consider the DCS of two identical circular cylinders located on the X axis as shown in Fig. 9; we obtain the results shown in Fig. 10, and again the agreement between the two methods is excellent.

B. Numerical Efficiency and Accuracy of the Fast Fourier Factorization Method

In this subsection we discuss in more detail the numerical efficiency of the FFF method. For the structures already studied (Figs. 7 and 9), the single-cylinder case is in fact more difficult to model than the two-cylinder case. Consequently, we focus on this demanding structure for our convergence tests. In Fig. 11 we show the DCS of the single cylinder for $\theta=30^\circ$ versus the development order N for several values of the number of S -algorithm slices. We give both the classical differential method⁷ and the FFF method results. We clearly see that the FFF method is more accurate than the classical differential method. For this angle of 30° and for both methods, we also see that an increase of the number of slices in the S algorithm improves the results. In Fig. 12 we give the same study but for $\theta=150^\circ$. Once again, the FFF method converges more

quickly than the classical method. Note that, as for $\theta=30^\circ$, the possible crossings between the line corresponding to the value computed with the MM and the convergence curves for small N values are not meaningful. Only the global behavior of these convergence curves are useful. To avoid such putative crossings in our convergence study, we give in Fig. 13 the average relative errors between the computed DCS values and the MM one for all the angles in the range $[0^\circ, 360^\circ]$. The improvement brought by the FFF method is evident (note the log scale on the Y axis). We finally obtain a relative difference of 2.10^{-4} between the FFF method results and the MM ones for $N=140$ and $L=55$. The results obtained with the FFF method are less accurate than the ones obtained with the MM for the different examples of DCS shown in Figs. 11 and 12. Nevertheless, the relative discrepancies between the two methods are fully acceptable. One can ask why such differences can still be observed whereas both the FFF method and the MM are rigorous methods, in which the unique approximations are the truncations of the used series. For the FFF method, we need to truncate the Fourier series of the electromagnetic fields (four components are needed to describe them in a conical mounting) and the ones of the permittivity of the diffracting device. In the case of the MM, we have to truncate only the

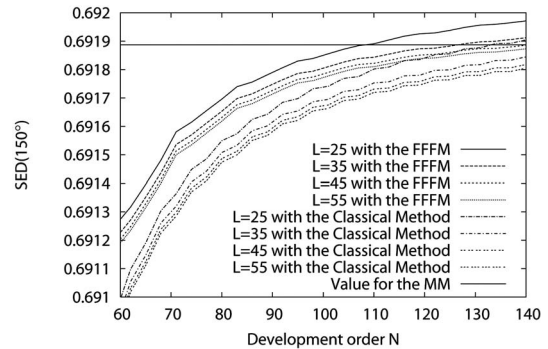


Fig. 12. Convergence test according to the order of the truncated Fourier series (N) of the point at 150° in the DCS of the FFF method (FFFM) (illustrated by Fig. 8) and of the classical differential method with $\lambda_0=1 \mu\text{m}$ and with different values of L (number of slices for the S algorithm) compared with the MM value.

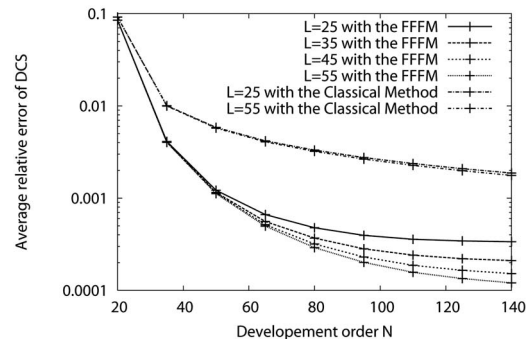


Fig. 13. Average relative error between the DCS of the FFF method (FFFM) (illustrated by Fig. 8) and of the classical differential method and the DCS of the MM according to the order of the truncated Fourier series (N) with $\lambda_0=1 \mu\text{m}$ and with different values of L (number of slices for the S algorithm).

Fourier–Bessel series of two field components (E_z and H_z are needed in conical mounting) since any series are needed of the permittivity. There are at least two other reasons explaining the better accuracy of the MM for the examples shown here. First, for homogeneous and circular inclusions, the reflection matrix relating the incident and the scattered field in the MM are known analytically. On the contrary, in the framework of the FFF, the inclusions are described through the permittivity tensor $\bar{\epsilon}$ (more precisely by its Fourier components) in the modulated area. Second, there is a crucial difference between the two methods: for the MM no numerical integration is necessary, while resolution such as the one associated with Eq. (26) of the FFF method requires such an integration; only analytical changes of basis using Graf's theorem^{2,10} are used for the rewriting of the Fourier–Bessel series, which lead to an explicit linear problem.

All these reasons also explain why the MM is much faster than the FFF method for the homogeneous and circular examples treated in this study, even if all the numerical computations can still be achieved on a single PC. It is worth considering how the MM accuracy evolves when noncircular inclusions are considered, and hence when a numerical integration is required. The results given in Ref. 11 concerning homogeneous and elliptical inclusions can give us a first evaluation since a numerical integration is required to compute the reflection matrix of the ellipses. The final results obtained by the MM lose approximately three significant digits when these noncircular inclusions are studied. We do not observe such worsening of the accuracy within the FFF method when similar ellipses are considered instead of circular inclusions since the circles are not treated differently than the ellipses.

To conclude this subsection, we remind the reader that circular and homogeneous inclusions are a special case in which the Multipole Method is certainly the best possible numerical method since several steps are done analytically. The purpose of the FFF method is not to study such simple, but more complicated structures; a trade-off is obtained between the accuracy speed and the generality of the studied structures.

C. Devices with Subperiodicity According to θ

As with MOFs, any device may present a cross section with a subperiodicity according to θ . This property can be taken into account in the integration process to reduce the computation time. Let us assume that the device presents a subperiod T such that $N_T T = 2\pi$ where N_T is the number of periodicity. Thus the spectra of the functions $\epsilon(r, \theta)$ and $N_\theta^2(r, \theta)$ are wider than those obtained without subperiodicity. More precisely, we consider a function $\tilde{f}(\theta)$ (ϵ , N_θ^2 or $N_r N_\theta$) subperiodic with period T . The Fourier coefficients of \tilde{f} on the 2π range \tilde{f}_n ($\forall n \in \mathbb{N}$) and the Fourier coefficients of \tilde{f} on the T range \tilde{f}'_n ($\forall n \in \mathbb{N}$) are linked by the following relations: if $n = kN_T$ ($\forall k \in \mathbb{N}$), then $\tilde{f}_n = \tilde{f}'_k$ and $\tilde{f}_n = 0$ otherwise. Consequently, the Toeplitz matrix of the function \tilde{f} is made of nonnull diagonals regularly separated by $N_T - 1$ null diagonals. For instance, if $N = 4$ and $N_T = 3$, the Toeplitz matrix of the function \tilde{f} is

$$\mathbb{[\tilde{f}]} = \begin{bmatrix} \tilde{f}'_0 & 0 & 0 & \tilde{f}'_1 & 0 & 0 & \tilde{f}'_2 & 0 & 0 \\ 0 & \tilde{f}'_0 & 0 & 0 & \tilde{f}'_1 & 0 & 0 & \tilde{f}'_2 & 0 \\ 0 & 0 & \tilde{f}'_0 & 0 & 0 & \tilde{f}'_1 & 0 & 0 & \tilde{f}'_2 \\ \tilde{f}'_{-1} & 0 & 0 & \tilde{f}'_0 & 0 & 0 & \tilde{f}'_1 & 0 & 0 \\ 0 & \tilde{f}'_{-1} & 0 & 0 & \tilde{f}'_0 & 0 & 0 & \tilde{f}'_1 & 0 \\ 0 & 0 & \tilde{f}'_{-1} & 0 & 0 & \tilde{f}'_0 & 0 & 0 & \tilde{f}'_1 \\ \tilde{f}'_{-2} & 0 & 0 & \tilde{f}'_{-1} & 0 & 0 & \tilde{f}'_0 & 0 & 0 \\ 0 & \tilde{f}'_{-2} & 0 & 0 & \tilde{f}'_{-1} & 0 & 0 & \tilde{f}'_0 & 0 \\ 0 & 0 & \tilde{f}'_{-2} & 0 & 0 & \tilde{f}'_{-1} & 0 & 0 & \tilde{f}'_0 \end{bmatrix}. \quad (47)$$

We notice that the matrix $\mathbb{[\tilde{f}]}$ is block diagonalizable. This matrix structure is preserved when such a matrix is reversed or when two such matrices are multiplied; that is why every block of the integration matrix $M(r)$ given by Eq. (26) has this matrix structure. Finally, we conclude that Eq. (26) is split into N_T independent differential sets with matrix sizes equal to $4(2N+1)/N_T$ or less. Since the integration computation time depends roughly on the cube of the matrix integration size, the time of a successive integration of each differential subset scales as $N_T(4(2N+1)/N_T)^3 = (4(2N+1))^3/N_T^2$, while the time of the global differential set [Eq. (26)] scales as $(4(2N+1))^3$. It means that taking into account the subperiodicity according to θ of the diffracting surface permits us to gain a factor of N_T^2 on the computation time. Moreover, each differential subset depends on the reduced Toeplitz matrix:

$$\mathbb{[\tilde{f}']} = \begin{bmatrix} \tilde{f}'_0 & \tilde{f}'_1 & \tilde{f}'_2 \\ \tilde{f}'_{-1} & \tilde{f}'_0 & \tilde{f}'_1 \\ \tilde{f}'_{-2} & \tilde{f}'_{-1} & \tilde{f}'_0 \end{bmatrix},$$

which simplifies the calculation of the Fourier developments of ϵ , N_θ^2 , and $N_r N_\theta$ functions defined only on the T period. The subperiodicity according to θ was first successfully implemented on an elliptical cross-section surface centered to the origin since it is π periodic ($N_T=2$) and then on the circular cylinder defined on a period T (data not shown). We note that this study on subperiodicity can be linked to the seminal work of McIsaac¹² concerning waveguide symmetry properties and with the paper written by Bai and Li.¹³ The authors of Ref. 13 have explicitly shown how the use of group theory permits one to fairly reduce the computation time on crossed grating analysis. More recently, Fini¹⁴ has revisited McIsaac's work to improve the efficiency of several numerical methods if rotational symmetry properties are present in the device.

D. Excitation of the Fundamental Leaky Mode of a Microstructured Optical Fiber

The subperiodicity of the diffracting device is particularly useful in the case of MOFs. These fibers are usually made of several rings of circular cylinders (filled with vacuum) regularly distributed according to the angular coordinate θ in a infinite matrix. We thus consider a solid core MOF (Fig. 14) composed of six identical circular cylinders with

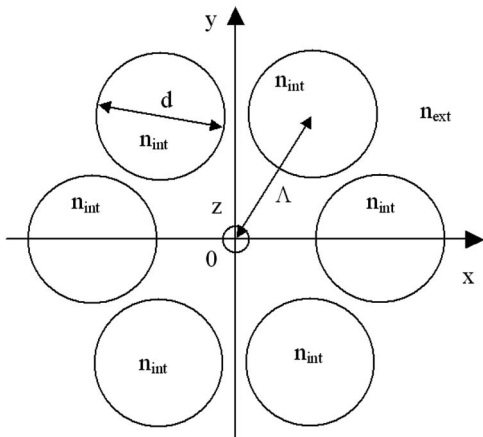


Fig. 14. Cross section of a MOF composed of six identical circular cylinders with $d=1 \mu\text{m}$, $\Lambda=2.3 \mu\text{m}$, $n_{\text{int}}=1$, and $n_{\text{ext}}=1.4439$.

a diameter $d=1 \mu\text{m}$ and the same distance to the origin (pitch) $R_0=\Lambda=2.3 \mu\text{m}$ ($\theta_0=0^\circ$); it means that the subperiod is $2\pi/6$ ($N_T=6$). In addition, the whole structure has symmetry planes, so in the formulation used in waveguide theory,¹² this fiber follows the C_{6v} symmetries. The cylinder index is $n_{\text{int}}=1$ and the matrix index is $n_{\text{ext}}=1.44390356$. In our notation [Eq. (3)], the parameter γ_0 becomes the studied propagation constant usually noted as β . The effective index is defined by $n_{\text{eff}}=\beta/k_0$. The well-established MM¹⁻³ can also be formulated as a modal method, and consequently it can find the modes of MOFs composed with arbitrary inclusions contained in disjointed circular cylinders. It gives a complex effective index equal to $n_{\text{eff}}=1.420784+i7.20952 \times 10^{-4}$ with $\lambda_0=1.56 \mu\text{m}$ for the fundamental mode, i.e., this mode is a leaky mode (even if the optical indices of the inclusions and the matrix are purely real). In addition, we know that the fundamental mode is twice degenerated.^{1,12} Its component fields E_z belong either to the C4 symmetry class [symmetric according to the Y axis, $u(\pi-\theta)=u(\theta)$, and antisymmetric according to the X axis, $u(-\theta)=-u(\theta)$] or to the C3 symmetry class (antisymmetric according to the Y axis and symmetric according to the X axis). This classification of symmetry is more precisely explained in the work of McIsaac.¹² We search now to apply these symmetry properties on the diffracting problem. The mode that belongs to the C3 symmetry class is excited when $\theta_{\text{inc}}=90^\circ$ and the second one (C4 symmetry class) when $\theta_{\text{inc}}=0^\circ$.

In the framework of our diffraction method, we have first tried to excite the fundamental mode described above with suitable incident wave parameters [Eq. (1)]. We know that the real parameter γ_0 is equal to $-k_{\text{ext}} \sin(\varphi)$ in which $k_{\text{ext}}=k_0 n_{\text{ext}}$; hence we have searched the angle parameter φ such that $\gamma_0=k_0 \text{Re}(n_{\text{eff}})$, and we have approximately found $\varphi=-79.73^\circ$ about [$\varphi=-\arcsin(\text{Re}(n_{\text{eff}})/n_{\text{ext}})$]. Doing so, we have neglected the imaginary part of n_{eff} . Consequently, the fundamental mode is only partially excited. Figure 15 shows the computation time versus N for both the six circular cylinder MOFs defined on the 2π period and for the one defined on the $T=2\pi/6$ period. These results clearly illustrate the improvement brought about by the subperiodicity concerning the computation time. Figure 16 illustrates the normalized $|E_z|$ map associated with the partial excitations of the fundamental mode be-

longing to the C3 symmetry class and Fig. 17 to the C4 symmetric class ($N=60$ and $\phi=0^\circ$). The fields seem well located around the circular cylinders and the similarity with the MM¹ field maps is already clear even if the result

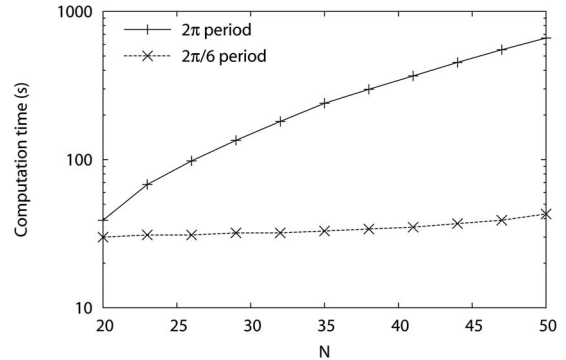


Fig. 15. Computation time for the six circular cylinders as a function of the order of the truncated Fourier series (N), with and without taking advantage of the symmetry.

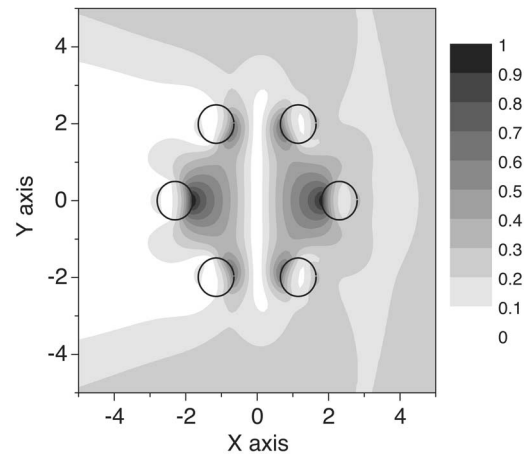


Fig. 16. Normalized $|E_z|$ field map obtained thanks to the partial excitation (see Fig. 18 for the complete excitation) of the MOF fundamental mode belonging to the C3 symmetry class [$\theta_{\text{inc}}=90^\circ$, $\phi=0^\circ$, $\lambda_0=1.56 \mu\text{m}$, $N=60$, and $\gamma_0=k_0 \text{Re}(n_{\text{eff}})=1.420784$]. The studied fiber is the same as in Fig. 14.

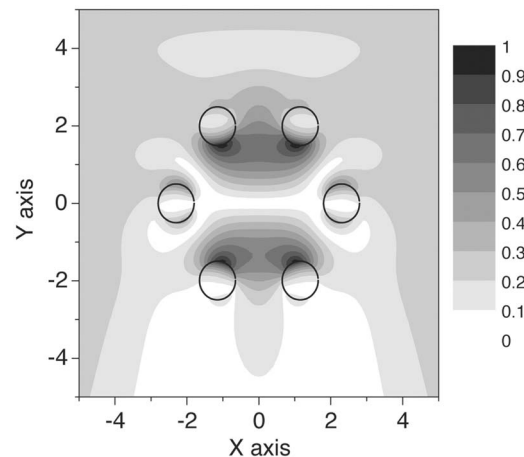


Fig. 17. Normalized $|E_z|$ field map obtained thanks to the partial excitation (see Fig. 19 for the complete excitation) of the MOF fundamental mode belonging to the C4 symmetry class ($\theta_{\text{inc}}=0^\circ$). The studied fiber is the same as in Fig. 14.

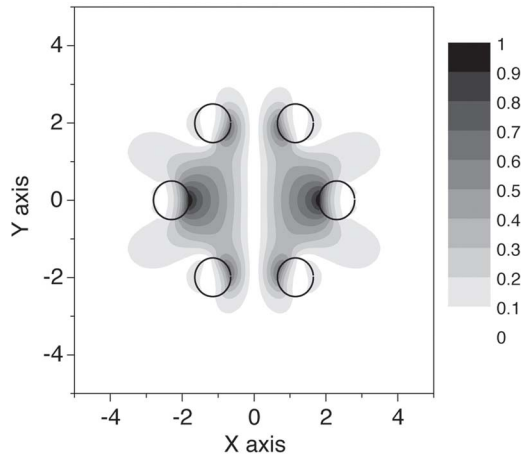


Fig. 18. Normalized $|E_z|$ field map obtained thanks to the complete excitation (see Fig. 16 for the partial excitation) of the MOF fundamental mode belonging to the C3 symmetry class ($\theta_{\text{inc}}=90^\circ$, $\phi=0^\circ$, $\lambda_0=1.56 \mu\text{m}$, $N=60$, and $\gamma_0=k_0 n_{\text{eff}}=1.420784+i7.20952 \times 10^{-4}$). The studied fiber is the same as in Fig. 14.

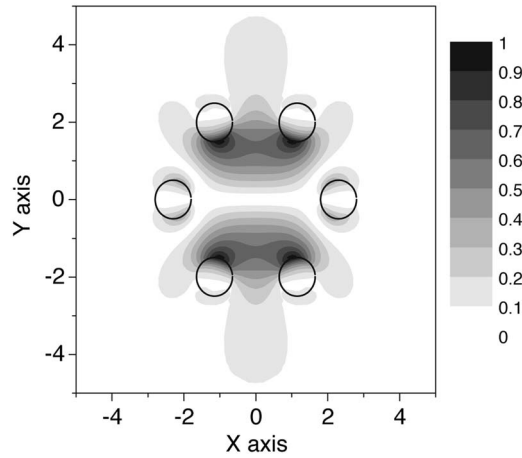


Fig. 19. Normalized $|E_z|$ field map obtained thanks to the complete excitation (see Fig. 17 for the partial excitation) of the MOF fundamental mode belonging to the C4 symmetry class ($\theta_{\text{inc}}=0^\circ$; other parameters are identical to the ones of Fig. 18) of the fundamental mode. The studied fiber is the same as in Fig. 14.

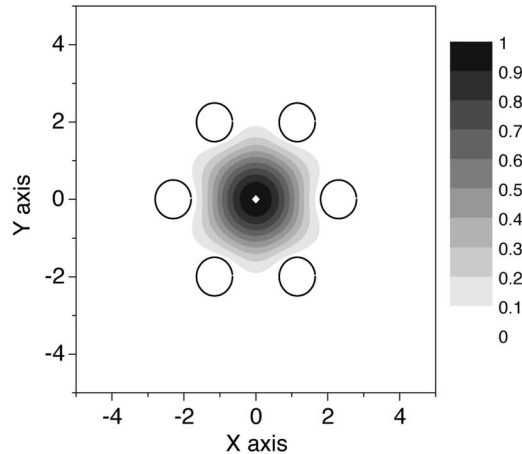


Fig. 20. Normalized $|S_z|$ field map computed from the electromagnetic fields associated with Fig. 18 (the result is similar when the results associated with Fig. 19 are considered).

shown in Fig. 16 is a diffraction phenomenon and not a true mode.

To excite completely the fundamental mode by a incident wave, we now take into account the imaginary part of n_{eff} . The complex number $\gamma_0=k_0 n_{\text{eff}}$ implies that φ also becomes a complex number. However, this implies that all the components of the incident fields are proportional to the same complex number $\cos(\varphi)$. In this case, the field amplitudes $A_{e,z}$ and $A_{h,z}$ deduced from Eq. (2) also become complex numbers proportional to $\cos(\varphi)$:

$$A_{e,z} = \cos(\varphi)\cos(\phi)|\mathbf{E}^{(\text{inc})}|, \quad (48)$$

$$A_{h,z} = \frac{1}{Z} \cos(\varphi)\sin(\phi)|\mathbf{E}^{(\text{inc})}|. \quad (49)$$

Since all the other incident field components are proportional to $A_{e,z}$ and $A_{h,z}$, they are also proportional to $\cos(\varphi)$. Consequently, it is not even necessary to determine the $\cos(\varphi)$ factor if we are only interested in normalized fields. In our example, we choose $\gamma_0=k_0 n_{\text{eff}}$. Figures 18 and 19 show the normalized $|E_z|$ maps associated with the accurate excitation of the C3 (and C4) symmetry class mode, respectively. Figure 20 illustrates the modulus of the z component of the Poynting vector noted as S_z for both electromagnetic field maps ($N=60$). We recognize the same field maps as the ones obtained with the MM used in its mode-searching operation.¹

6. CONCLUSION

The described FFF method introduces Toeplitz matrices for permittivity $[\epsilon]$ and $[1/\epsilon]$ and also Toeplitz matrices for geometric quantities such as the normal vector components of the diffracting surface: $[N_\theta^2]$, $[N_r^2]$, and $[N_\theta N_r]$. The convergence results depend directly on these matrix conditions. The numerical implementation on the circle case in which the $\epsilon(r, \theta)$ and $N_\theta^2(r, \theta)$ functions present important variations according to θ shows satisfying results for $N=50$. Moreover, the integration of the differential set in the modulated area fairly simplifies when the possible subperiodicity of the diffracting device is taken into account. We apply the FFF method to simple structures made of circular inclusions so as to be able to compare it with a known method. However, the FFF method described here in cylindrical coordinates can compute the fields diffracted by more complex structures than the ones shown in this present work: Some other different diffracting surfaces have been successfully studied (elliptical cylinder, rectangular cylinder, etc.), and the most general case of anisotropic and/or inhomogeneous media can also be analyzed. An association between the FFF method in the homogeneous and isotropic case and the MM has already been used to study a MOF with elliptical inclusions.¹¹ Our future work will deal with the adaptation of the FFF method applied to light diffraction to the search of modes into arbitrary cross-section MOFs to overcome the known limitations of the MM¹ (inclusions must be inscribed in nonoverlapping circles, the matrix

permittivity must be homogeneous). In this case, the diffraction problem becomes an homogeneous problem, i.e., an eigenvalue problem.

ACKNOWLEDGMENTS

The support of the European Community-funded project PHOREMOST (FP6/2003/IST/2-511616) is gratefully acknowledged. The content of this work is the sole responsibility of the authors. We thank the Free Software Foundation and the Scilab Consortium for their help.

REFERENCES

1. F. Zolla, G. Renversez, A. Nicolet, B. Kuhlmeiy, S. Guenneau, and D. Felbacq, *Foundations of Photonic Crystal Fibers* (Imperial College Press, 2005).
2. T. P. White, B. T. Kuhlmeiy, R. C. McPhedran, D. Maystre, G. Renversez, C. M. de Sterke, and L. C. Botten, "Multiple method for microstructured optical fibers. I. Formulation," *J. Opt. Soc. Am. B* **19**, 2322–2330 (2002).
3. B. T. Kuhlmeiy, T. P. White, G. Renversez, D. Maystre, L. C. Botten, C. M. de Sterke, and R. C. McPhedran, "Multipole method for microstructured optical fibers. II. Implementation and results," *J. Opt. Soc. Am. B* **19**, 2331–2340 (2002).
4. M. Nevière and E. Popov, *Light Propagation in Periodic Media: Differential Theory and Design* (Marcel Dekker, 2003).
5. P. Boyer, E. Popov, M. Nevière, and G. Tayeb, "Diffracting theory in TM polarization: application of the fast Fourier factorization method to cylindrical devices with arbitrary cross section," *J. Opt. Soc. Am. A* **21**, 2146–2153 (2004).
6. M. Nevière, "The homogeneous problem," in *Electromagnetic Theory of Gratings*, R. Petit ed. (Springer-Verlag, 1980).
7. P. Vincent and R. Petit, "Sur la diffraction d'une onde plane par un cylindre diélectrique," *Opt. Commun.* **5**, 261–266 (1972).
8. L. Li, "Use of Fourier series in the analysis of discontinuous periodic structures," *J. Opt. Soc. Am. A* **13**, 1870–1876 (1996).
9. L. Li, "Formulation and comparison of two recursive matrix algorithms for modeling layered diffraction gratings," *J. Opt. Soc. Am. A* **13**, 1024–1035 (1996).
10. M. Abramowitz and L. E. Stegun, eds., *Handbook of Mathematical Functions with Formulas, Graphs, and Mathematical Tables* (National Bureau of Standards, 1972).
11. S. Campbell, R. C. McPhedran, C. M. de Sterke, and L. C. Botten, "Differential multipole method for microstructured optical fibers," *J. Opt. Soc. Am. B* **21**, 1919–1928 (2004).
12. P. R. Melsaac, "Symmetry-induced modal characteristics of uniform waveguides. I. Summary of results," *IEEE Trans. Microwave Theory Tech.* **MTT-23**, 421–429 (1975).
13. B. Bai and L. Li, "Reduction of computation time for crossed-grating problems: a group-theoretic approach," *J. Opt. Soc. Am. A* **21**, 1886–1894 (2004).
14. J. M. Fini, "Improved symmetry analysis of many-moded microstructure optical fibers," *J. Opt. Soc. Am. B* **21**, 1431–1436 (2004).